Simulating aerosol-radiation effects on subseasonal prediction using the coupled Unified Forecast System and CCPP-Chem: prescribed aerosol climatology versus interactive aerosol model

S. Sun[1], G. A. Grell[1], L. Zhang[1,2], J. K. Henderson[1], S. Wang[2,3], D. Heinzeller[4], H. Li[1,2], J. Meixner[5], P. S. Bhattacharjee[6]

[1]NOAA Global Systems Laboratory
[2]University of Colorado at Boulder, Cooperative Institute for Research in Environmental Sciences
[3]NOAA Chemical Sciences Laboratory
[4]University Corporation for Atmospheric Research (UCAR) / UCAR Community Programs / Joint Center for Satellite Data Assimilation
[5]NOAA NCEP Environmental Modeling Center (EMC)
[6]SAIC at NCEP EMC

Key Points:

- The incorporation of aerosol-radiation interaction (ARI) in the coupled atmosphere-ocean-sea ice model UFS-CCPP-Chem indicates a net cooling effect at the top of the atmosphere on subseasonal prediction
- Two simulations, one with an interactive aerosol model and the other using the prescribed aerosol climatology, demonstrated comparable ARI effects and corresponding meteorological impacts on weekly and monthly scales
- Substituting the interactive aerosol model with the aerosol climatology presents a cost-effective alternative in subseasonal applications

Corresponding author: Shan Sun, Shan.Sun@noaa.gov

Abstract

This study investigates the effects of aerosol-radiation interaction on subseasonal prediction using the Unified Forecast System (UFS) with an ocean, a sea ice and a wave component, coupled to an aerosol component. The aerosol component is from the current NOAA operational GEFSv12-Aerosols model, which includes the GOCART aerosol modules simulating sulfate, dust, black carbon, organic carbon, and sea-salt. The modeled aerosol optical depth (AOD) is compared to reanalysis from Modern-Era Retrospective analysis for Research and Applications, Version 2 (MERRA2) and observations from Moderate Resolution Imaging Spectro-radiometer (MODIS) satellite and Atmospheric Tomography (ATom) aircraft. Despite biases primarily in dust and sea salt, a good agreement in AOD is achieved globally. The simulated radiative forcing (RF) from the total aerosols at the top of the atmosphere is approximately -2.5 W/m^2 or -16 W/m^2 per unit AOD globally. This is consistent with previous studies.

In subsequent simulations, prognostic aerosol component is substituted with climatological aerosol concentrations derived from initial experiments. While regional differences in RF are noticeable in specific events between these two experiments, the resulting RF, surface temperature, geopotential height at 500 hPa and precipitation, show similarities in multi-year subseasonal applications. This suggests that given the current capacities of the aerosol modeling, adopting a climatology of aerosol concentrations as a cost-effective substitute for the intricate aerosol module may be a practical approach for subseasonal applications.

Plain Language Summary

This research explores how the interaction between aerosols and radiation influences weather predictions over several weeks. Our forecast system consists of six components, including the atmosphere, land, ocean, sea ice, wave and aerosols. Despite some differences, the simulated aerosol optical depth aligns with observations. The impact of these aerosols on the Earth's energy balance results in a net cooling effect.

Furthermore, we conduct parallel experiments to assess a simpler method: prescribing aerosol climatology instead of utilizing an interactive aerosol model. We find numerous similarities in its influence on radiation at the top of the atmosphere and on meteorology at the subseasonal timescale between these two approaches, despite the absence of interannual variabilities in the aerosol climatology. Our findings suggest that adopting this simplified approach of prescribing aerosol climatology for subseasonal predictions might offer cost-saving benefits without compromising accuracy.

1 Introduction

Climate change is driven by changes in the earth's energy budget, which can be quantified by the radiative forcing (RF) measured at the top of the atmosphere (e.g., IPCC, 2013). A positive RF indicates that the earth system is absorbing energy. The largest increase in RF in recent years has been from the concentration of well-mixed greenhouse gases (GHGs) in the atmosphere, estimated to be 2.8 W/m^2 for 2011 or 3.3 W/m^2 for 2019 relative to 1750 (IPCC, 2013, 2021), where the total aerosol effective RF which includes the interaction of aerosols with solar radiation and cloudiness, partially offsets this positive RF with negative estimates of -0.9 W/m^2 for 2011 or –1.1 W/m^2 for 2019.

Atmospheric aerosols have an impact on weather and climate by interacting with solar radiation through scattering and absorbing light, affecting the three-dimensional temperature fields in the direct effect and influencing cloud properties, cloudiness, and precipitation in the indirect effect. Any changes in cloud properties resulting from aerosol-radiation interaction are classified as the semi-direct effect (e.g., J. M. Mitchell, 1971;

Twomey, 1974; IPCC, 2013). Aerosols originate from both natural and anthropogenic sources and are removed from the atmosphere by precipitation and other processes within a few days or weeks. Due to different aerosol species and particle sizes, they interact with climate in a far more complicated manner than GHGs.

Climate models have integrated aerosol effects for several decades with varying complexity (e.g., Hansen et al., 1992; Le Treut et al., 1998; Ming et al., 2005; Stier et al., 2005). It is only with the recent development of online modeling systems that showed the importance of aerosol direct effects in numerical weather prediction (NWP) models (e.g., Grell & Baklanov, 2011; Reale et al., 2011; Baklanov et al., 2014). For instance, including radiative effects of dust aerosols improved the radiation balance of NWP models (Haywood et al., 2005; Pérez et al., 2006) and helped forecast of African easterly Jet (Tompkins et al., 2005; Reale et al., 2011). Rodwell and Jung (2008) demonstrated an improvement in local medium-range forecast skill and a reduction in mean extratropical circulation errors in the ECMWF simulations when a more realistic dust aerosol climatology was employed. Grell et al. (2011) showed that aerosols resulting from wildfires had a significant influence on NWP, using the Weather Research and Forecasting model coupled with Chemistry (WRF-Chem, Grell et al., 2005; Fast et al., 2006) with complex chemistry and direct/indirect effects. Haustein et al. (2012) provided evidence of a connection between dust emissions and weather patterns over synoptic-to-seasonal time scales. Mulcahy et al. (2014) noted large regional improvements in radiation and temperature forecasts from the direct and indirect effects of aerosols in the Met Office's Unified Model for NWP, and recommended choosing an appropriate level of aerosol complexity that fits its applications. Furthermore, aerosol effects have also been shown to impact extreme weather events, such as tornadoes and hurricanes, in weather forecast models (e.g., Sun et al., 2008; Reale et al., 2014; Saide et al., 2015; Pan et al., 2020). Recently, Murakami (2022) quantified the impact of anthropogenic aerosols on tropical cyclone activity using the System for Prediction and Earth System Research (SPEAR) model from Geophysical Fluid Dynamics Laboratory (GFDL). Benedetti and Vitart (2018) investigated the potential of including interactive aerosols to improve monthly prediction in the ECMWF's IFS system, with a hypothesis that aerosol variability is connected to the different phases of the Madden–Julian oscillation (Madden & Julian, 1971).

Despite a large uncertainty in aerosol observations and modeling (Carslaw et al., 2013; Mann et al., 2014; Reddington et al., 2017; Vogel et al., 2022), substantial progress has been made in global aerosol modeling for operational aerosol forecasts. For instance, the International Cooperative for Aerosol Prediction (ICAP) project with nine global aerosol models has shown a higher skill in the multi-model ensemble mean than in the individual model (Reid et al., 2011; Xian et al., 2019), even though it does not consider aerosol feedback on meteorology. ICAP has paved the way for establishing quasi-real time aerosol reanalysis from multi-model ensembles for numerical weather prediction (NWP) applications. On the other hand, there is an ongoing debate regarding the computational cost of modeling interactive aerosol impact compared to the benefits and whether using some form of aerosol climatology or reanalysis is feasible. This is one question we attempt to address in this study from the perspective of aerosol-radiation interaction on subseasonal applications.

The WMO Working Group on Numerical Experimentation (WGNE) initiated a project to evaluate the impacts of aerosols on numerical weather prediction. The project examined how dust, smog and smoke scenarios affected surface radiation and temperature with eight models from six countries, including several operational NWP models (S. Freitas et al., 2015). Currently, the WGNE Aerosol project is in its second phase, focused on evaluating the impact of aerosols on subseasonal prediction (Frassoni et al., 2021). Our study is part of this project, and we use the coupled Unified Forecast System (UFS), NOAA's next operational coupled atmosphere-ocean-sea ice-land system for S2S predictions. Our goal is to document these experiments with detailed analysis of the aerosol radiative ef-

fects on S2S prediction. The experimental setup is described in Section 2. Section 3 presents the results of the aerosol-radiation interaction analysis on both the global and regional scales, where two-way feedback between aerosols and meteorology is simulated with either an interactive aerosol model or a prescribed aerosol climatology. A summary and conclusion of findings are presented in Section 4.

2 Model Setup and Experiments

This study investigates the radiative forcing of direct and semi-direct aerosol-radiation interaction in the UFS using the GFDL single-moment microphysics parameterization. The indirect impact between aerosols and clouds is not considered here but will be the subject of future experiments when a double-moment microphysics parameterization is used.

2.1 Model Components

A community effort, including major contributions from the Environmental Modeling Center (EMC) at the National Centers for Environmental Prediction (NCEP), is underway in developing the UFS for seamless weather prediction across time scales, ranging from short-range to seasonal. The UFS model framework comprises the GFDL Finite-Volume cubed-sphere dynamical core (FV3) (Harris et al., 2021), the Global Forecast System (GFS) physics package, the land surface model, the GFDL Modular Ocean Model MOM6 (Harris et al., 2021), the Sea Ice Model CICE from Los Alamos National Laboratory (Hunke et al., 2015) and the wave model WAVEWATCH III (Tolman et al., 2002). Its subseasonal forecast skills are evaluated in Stefanova et al. (2022) through a series of incremental prototypes. This study is based on the version of Prototype 6 (P6), which uses FV3 with the GFS physics package version 16 (GFSv16, NOAA, 2021) via the Common Community Physics Package (CCPP, Heinzeller et al., 2023), the Noah land surface model (K. Mitchell, 2005) and CICE6. We coupled a revised version of P6 to the aerosol component from the GEFSv12-Aerosols model as described in Zhang et al. (2022). Since the aerosol component is coupled inline using CCPP, we refer to the resulting model system as UFS-CCPP-Chem in this study, as shown in Table 1.

2.2 Aerosol Component

The aerosol component is based on WRF-Chem, which employs the aerosol modules from the NASA Goddard Chemistry Aerosol Radiation and Transport model (GOCART, Chin et al., 2000, 2002). Five species of aerosols are included in this study, which are sulfate, dust, black carbon (BC), organic carbon (OC) and sea-salt. GOCART uses a simplified sulfur chemistry for sulfate simulation, bulk aerosols of BC, OC, and sectional dust and sea-salt. GEFSv12-Aerosols updated the sea-salt scheme based on the 2nd-generation GOCART model (Colarco et al., 2010) and a new dust emission scheme called FENGSHA, with a distinct approach to treat biomass burning and dust emissions (Zhang et al., 2022). Both dust and sea-salt have five size bins.

During the inline coupling, the meteorological fields, including the land-sea mask, vegetation type, and surface fields, are imported from the atmospheric model to drive the aerosol component. The aerosol component updates the aerosol extinction coefficient, single scattering albedo, and asymmetry factor for each aerosol species and passes them to the radiation scheme in atmospheric physics.

The monthly anthropogenic emission inventories from the Community Emissions Data System based on 2014 inventory (CEDS-2014, Hoesly et al., 2018) are used. The daily fire emissions are obtained from the ECMWF Global Fire Assimilation System (GFAS, Kaiser et al., 2012), which assimilates fire radiative power observations from satellite-based sensors of NASA Terra Moderate Resolution Imaging Spectro-radiometer (MODIS,

Table 1. Model components, resolutions and initial conditions used in the UFS-CCPP-Chem experiments

Components	Modules	Resolutions	Initial Conditions
Atmosphere	FV3 & GFSv16	25km, 64 layers	CFSR May 1 & Sept. 1, 2003-2019
Ocean	MOM6	1/4°, 75 layers	CPC-3DVar (2011-2017) CFSR (other times)
Sea Ice	CICE6	1/4°	CPC-CSIS
Wave	WW3	1/2° x 1/2°	(rest)
Aerosol	GEFSv12-Aerosols	same as atmosphere	30-day free spin-up (from zero)

Levy et al., 2013; Sayer et al., 2014) and Aqua MODIS active fire products to produce daily estimates of emissions from wildfires and biomass burning. GEFSv12 Aerosols implements an updated one-dimensional time-dependent cloud module from WRF-Chem (Grell et al., 2011), which is also used at EMC in the High-Resolution Rapid Refresh (HRRR)-Smoke model to calculate injection heights and emission rates online (S. R. Freitas et al., 2007; Ahmadov et al., 2017). The resulting AOD from GEFSv12-Aerosols agrees well with satellite and aircraft observations in the short-range forecasts (Zhang et al., 2022; Bhattacharjee et al., 2023).

Regarding the cost estimate for the aerosol component, the CCPP version of the GEFSv12-Aerosols model (Zhang et al., 2022), with the same aerosol component used in the UFS-CCPP-Chem in this study, takes approximately 1129 core hours for a 7-day forecast at a standalone atmospheric configuration. This is nearly double the core hours of running the same model without the active aerosol component, which consumes 580 core hours. Both simulations employ 320 cores with an 8x8 grid layout and without coupling to ocean, ice and wave modules.

2.3 Initial Conditions, Ensemble Members and Resolutions

We followed the protocol from the WMO WGNE S2S (Frassoni et al., 2021), and initialized the model on May 1st and September 1st, respectively, from 2003 to 2019. The integration time is 32 days for all experiments. There are five ensemble members, in which the atmospheric initial conditions are time-shifted by up to ± 2 days, while the initial conditions for the rest of the modules remain the same.

Table 1 displays the resolution of the atmospheric and aerosol modules in the UFS-CCPP-Chem model, which are approximately 25km (C384) and consist of 64 vertical layers. The ocean model has a resolution of 1/4° horizontally and includes 75 vertical layers. The ice model shares the horizontal grid with the ocean model. The wave model is on the 1/2° x 1/2° grid. Atmospheric and oceanic initial conditions rely on CFSR (Saha et al., 2010), except for the years 2011-2017, when the ocean initial conditions used the 3DVar data from NCEP/CPC. NCEP/CPC also provides the sea ice initial conditions (CSIS, Liu et al., 2019). The wave model starts at rest. The aerosol initial conditions are from free spin-up runs by integrating the UFS-CCPP-Chem model for 30 days from zero aerosol concentration, prior to the scheduled initial date of May 1st or September 1st.

Table 2. Three sets of experiments used in this study.

Experiments	Aerosol Sources
Prognostic aerosols (*ProgAer*)	Aerosol module active (with prognostic aerosol)
Climatological aerosols (*ClimAer*)	Aerosol module inactive (use *ProgAer* monthly climatology)
No aerosols (*NoAer*)	Aerosol module inactive (no aerosol interaction considered)

2.4 Experimental Design

Climate and weather models can integrate aerosol effects in multiple ways, and three commonly practiced methods aim to reduce computational costs:

- Updating aerosol loadings as time changes,
- Using climatological aerosols that is fixed in time or vary with season or month,
- Ignoring aerosol loadings and its impact on meteorology.

This study evaluates and quantifies the radiative forcing from aerosols and the impact on meteorology, in each of these three options. The first set of experiments employs UFS-CCPP-Chem with 'prognostic aerosols' (*ProgAer*) that simulates the evolution of five tropospheric aerosol species, while enabling the aerosol feedback on radiation. Two more parallel sets of experiments are conducted with UFS but exclude the costly aerosol component. They utilize either prescribed climatological aerosol concentrations (*ClimAer*) or zero aerosol concentration (*NoAer*) instead of the aerosol module. Note that the climatological aerosol concentrations used in *ClimAer* is a monthly model climatology generated from Experiment *ProgAer*, as illustrated in Table 2. This is done to ensure that the mean aerosol concentrations in Experiments *ClimAer* and *ProgAer* are the same.

2.5 Observations from Satellites and Aircrafts

We verified our modeled AOD using the MODIS Collection 6.1 Level-3 AOD dataset (Levy et al., 2013) from the Aqua satellite, where the merged AOD product combines retrievals from the Dark Target and Deep Blue algorithms to provide a consistent data set that spans various surface types from oceans to bright deserts (Sayer et al., 2014). We compared each of the 5 modeled AOD components against the Modern-Era Retrospective analysis for Research and Applications, Version 2 (MERRA2, Buchard et al., 2017), which is an assimilation product of the Global Modeling and Assimilation Office at NASA.

The AOD dataset from the NASA Atmospheric Tomography Mission (ATom, Brock et al., 2021) comprises merged data from all instruments on aircraft flights during each of the four seasons from 2016 to 2018. It offers a comprehensive global-scale sampling of the atmosphere, profiling continuously from 0.2 to 12 km altitude and providing detailed latitude, longitude and altitude information. In this study we compared ATom-4 with our results, which overlaps with our experiments in May 2018.

We use the Clouds and the Earth's Radiant Energy System (CERES, Wielicki et al., 1996) data to validate radiative fluxes and cloud coverage in the model experiments. CERES provides global composite radiative fluxes, including top-of-atmosphere (TOA)

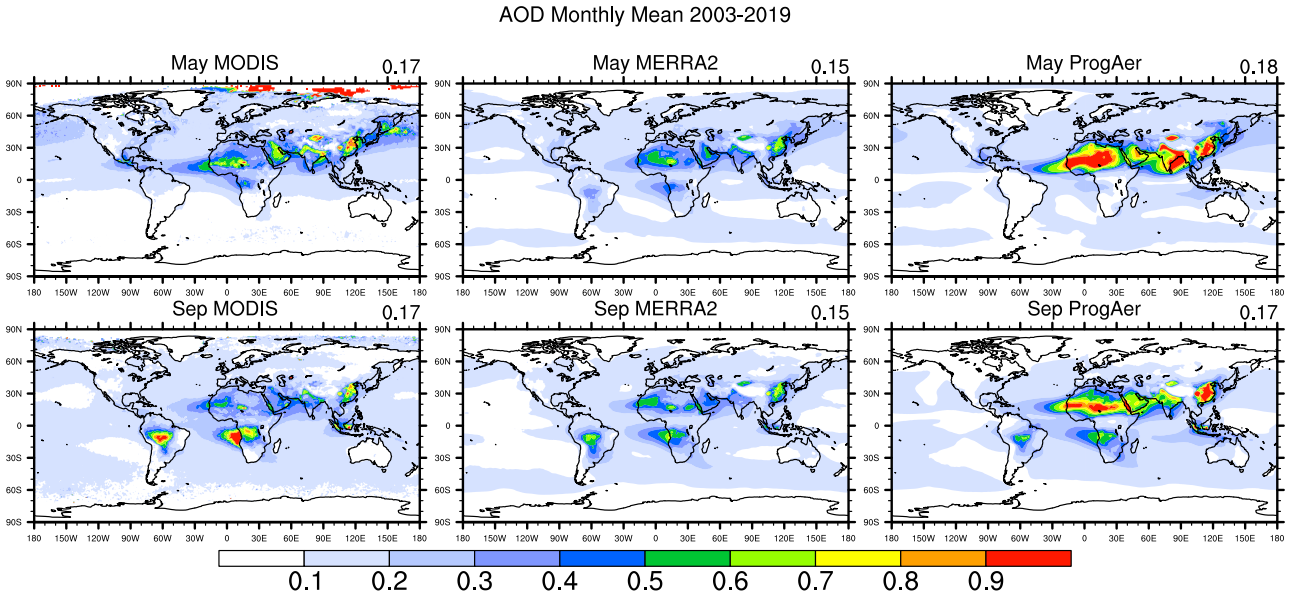

Figure 1. Monthly mean AOD at 550nm during 2003-2019 in May (upper) and September (lower) from MODIS (left), MERRA2 (middle) and Experiment *ProgAer* (right). Global mean is shown in the upper right corner.

shortwave and longwave, and cloud properties based on each CERES 20 km field of view. We employ the Edition 4.2 product of the CERES Energy Balance and Filled (EBAF) observations (Loeb et al., 2018) for the period of 2003-2019. The TOA fluxes and the cloud properties of CERES EBAF are monthly averages on a 1°x1° latitude-longitude grid. The estimated uncertainty in the regional monthly mean all-sky TOA flux ranges from 2.5 W/m^2 to 3 W/m^2 in this product.

The ERA5 global reanalysis (Hersbach et al., 2020) serves as the reference dataset for verifying the modeled surface temperature and geopotential height at 500 hPa (H500). Modeled precipitation is validated utilizing GPCP (Huffman et al., 2001), a composite dataset integrating in situ gauge data with satellite observations of daily precipitation.

3 Model Results and Comparison to Observations

All verification in each of the three experiments in this study is conducted using the ensemble means from the five members discussed earlier, after interpolated onto a 1° horizontal resolution.

3.1 Aerosol Optical Depth

Fig. 1 presents monthly averages of aerosol optical depth at 550 nm[1] from Experiment *ProgAer* compared with satellite estimates from MODIS and MERRA2 reanalysis for May and September during the period from 2003 to 2019. The modeled results

[1] All AODs in this manuscript are at 550 nm.

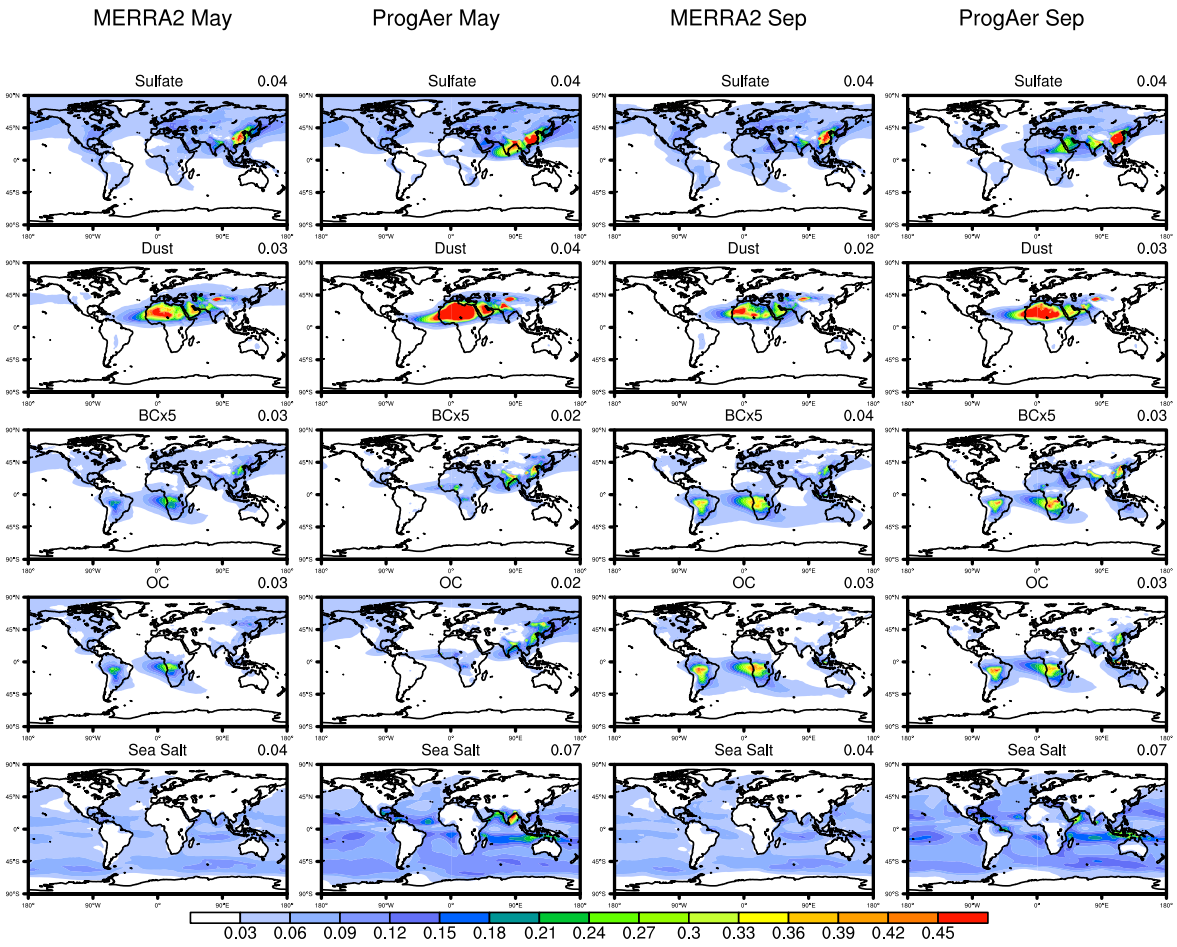

Figure 2. Each of the five components in AOD at 550 nm, sulfate, dust, BC, OC and sea-salt (top to bottom), from MERRA2 and Experiment *ProgAer* in May (left two rows) and September (right two rows) averaged over years 2003-2019. Note that BC AOD is enlarged by a factor of 5 in order to share the colorbar.

effectively captured the geographic patterns of AOD shown in MODIS and MERRA2, with positive biases in North Africa as well as South and East Asia. The AOD distribution between MODIS and MERRA2 shows good agreement in general, considering that MODIS is one of the various datasets assimilated by MERRA2. However, it is noteworthy that the magnitude of AOD from MERRA2 tends to be lower than that from MODIS across both months. Note that there are large values in MODIS over the Arctic region in May.

To further investigate the root in AOD bias, the five AOD components used in the models, namely sulfate, dust, BC, OC and sea-salt, are compared to MERRA2 in May and September in Fig. 2, using the 2003-2019 monthly averages. Among these five components, the biggest bias is in dust AOD over the Saharan region, where it has an excessive dust loading compared to MERRA2 in both months. This bias in the modeled dust AOD may be related to the bias in dust emission in the 'FENGSHA' scheme or in

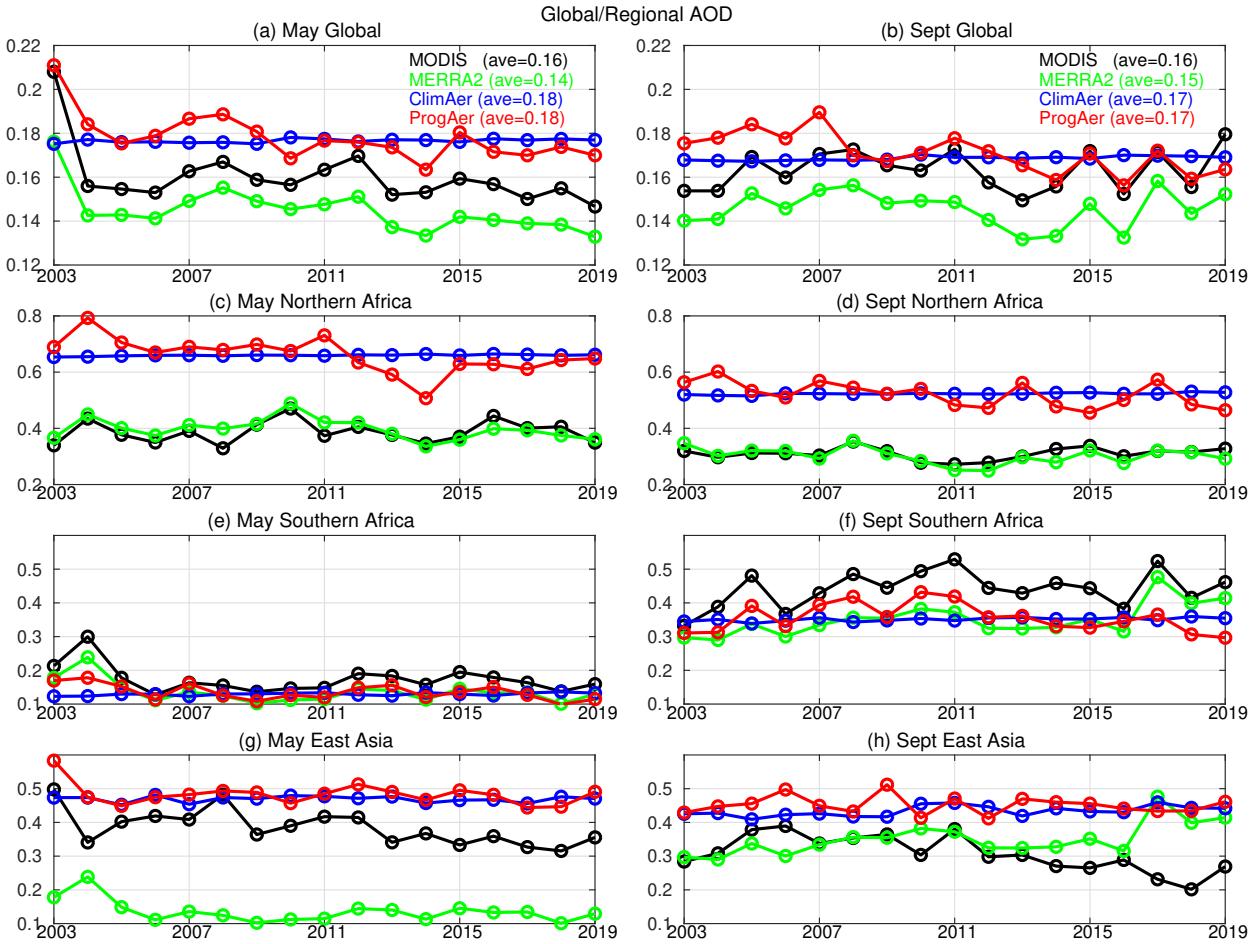

Figure 3. AOD at 550 nm in May (left) and September (right) during 2003-2019 from MODIS, MERRA2 and model experiments *ProgAer* and *ClimAer* globally and in three chosen regions of northern Africa (0 - 30°E, EQ - 30°N), southern Africa (0 - 30°E, EQ - 30°S) and east Asia (100°E - 130°E, 15°N - 45°N).

the modeled surface meteorology. The global mean sulfate AOD, shown in the upper right corner, is close to MERRA2, despite a larger local maximum over East Asia. The model underestimates OC/BC AOD in Central Africa and South America in May, likely from a weaker than observed biomass burning prescribed from the GFAS dataset. In contrast, the modeled sea-salt AOD is higher than MERRA2 over most of the ocean surface, particularly in the north Indian Ocean.

The global mean AOD values from MODIS, MERRA2, Experiments *ProgAer* and *ClimAer* are shown in the upper panel of Fig. 3 in May and September during the period from 2003 to 2019. The 17-year average for each product is listed in the upper right corner. The AOD from Experiment *ProgAer* shares a lot in common with that from MODIS, not only in the mean value but also in the interannual variabilities. As expected, the AOD from Experiments *ClimAer* is close to the average of that from Experiments *ProgAer* during this period, where the former uses the model climatology from the latter. The global mean AOD value from MERRA2 is the lowest among these products both in May and September during each of the 17 years. Additionally, Fig. 3 displays the area mean in several chosen regions with high AOD loading, including northern Africa (0 - 30°E, EQ - 30°N), southern Africa (0 - 30°E, EQ - 30°S) and east Asia (100°E - 130°E, 15°N - 45°N),

from MODIS, MERRA2 and Experiments *ProgAer* and *ClimAer*. The modeled AOD consistently exceeds satellite observations and reanalysis data in northern Africa in both May and September each year. This positive bias in AOD, primarily attributed to dust as shown in Fig. 2, contributes to the overall positive bias seen in the total AOD in the model experiments. Moreover, the AOD dominated by aerosols from biomass burning in southern Africa is much stronger in September than in May in all products. The modeled AOD over east Asia is relatively stable throughout the years and is somewhat higher than that from MODIS in both May and September, mostly from the sulfate components shown in Fig. 2.

The zonal mean AOD average of 2003-2019 and its standard deviation during this period are shown in the top panel of Fig. 4, for MODIS, MERRA2 and Experiment *ProgAer* in May and September. As shown in Fig. 1, one notable aspect is that the model tends to overestimate AOD between 10°N - 30°N, compared to MODIS. This bias mostly comes from dust and somewhat from sulfate, as shown in Fig. 2. The interannual variabilities of the zonal mean AOD in Experiment *ProgAer*, shown by the standard deviation, match that in MODIS and MERRA2. A larger interannual variability of AOD is seen in May at high latitudes in the Northern Hemisphere from Experiment *ProgAer*. To explore its root, zonal mean AOD from each of the five components, sulfate, dust, BC, OC and sea-salt, and their standard deviations are also shown in Fig. 4. It turns out that it is the OC component that has a large standard deviation north of 40°N, which indicates a large interannual variability of OC at mid-high latitudes in May. Among these five components, another source of discrepancy in AOD between the model and MERRA2 is in the sea-salt, which occurred at most latitudes where the ocean exists. The relatively small standard deviation in most region makes it feasible to have consistent results when using time-varying aerosols versus climatological aerosols.

Fig. 5 compares the total AOD and its components from Experiment *ProgAer* with a single flight circuit from the ATom-4 aircraft observations in the Pacific and Atlantic sections during May 2018. The modeled total AOD matches well with ATom-4 observations at all latitudes in the Pacific and Atlantic sections, except for a positive bias at high latitudes in the Pacific and an even larger positive bias at low latitudes in the northern Atlantic. The component analysis reveals that the modeled AOD from combined sulfate and OC mostly accounts for the large positive bias at high latitudes in the North Pacific and is in better agreement with ATom-4 in the Atlantic section, except for a spike near 45°N. The positive bias in the Atlantic mostly comes from dust between the equator and 20°N. The modeled sea-salt AOD has a positive bias at most latitudes in both ocean basins. The modeled BC AOD, despite being smaller in magnitude compared to other components, is close to that from ATom-4 in both ocean basins. All the findings here are consistent with those in Fig. 4, where comparisons are against MODIS and MERRA2.

In summary, the modeled AOD distributions in Experiment *ProgAer* with time-varying prognostic aerosols are generally consistent with satellite and aircraft observations as well as reanalysis estimates, albeit with some noticeable biases. For instance, the model tends to overestimate dust AOD in West Africa and offshore compared to MODIS and ATom-4 data. Additionally, the model's estimate of sea-salt AOD is higher over most ocean basins than what is observed by MODIS and ATom-4. The largest interannual variability in modeled OC AOD among all components in May over the northern mid to high latitudes is consistent with that in MERRA2 over a 17-year period, despite being higher than ATom-4 observations in 2018 over the North Pacific. In addition, the AOD from Experiment *ClimAer* with a prescribed monthly climatology of aerosol concentrations derived from Experiment *ProgAer*, closely aligns with the 17-year mean seen in the latter.

Table 3 presents a global mean comparison of the five AOD components between the modeling study in Chin et al. (2002) and Experiment *ProgAer*. The annual mean in 1990 from Chin et al. (2002) and the monthly mean averaged over 17 years from Exper-

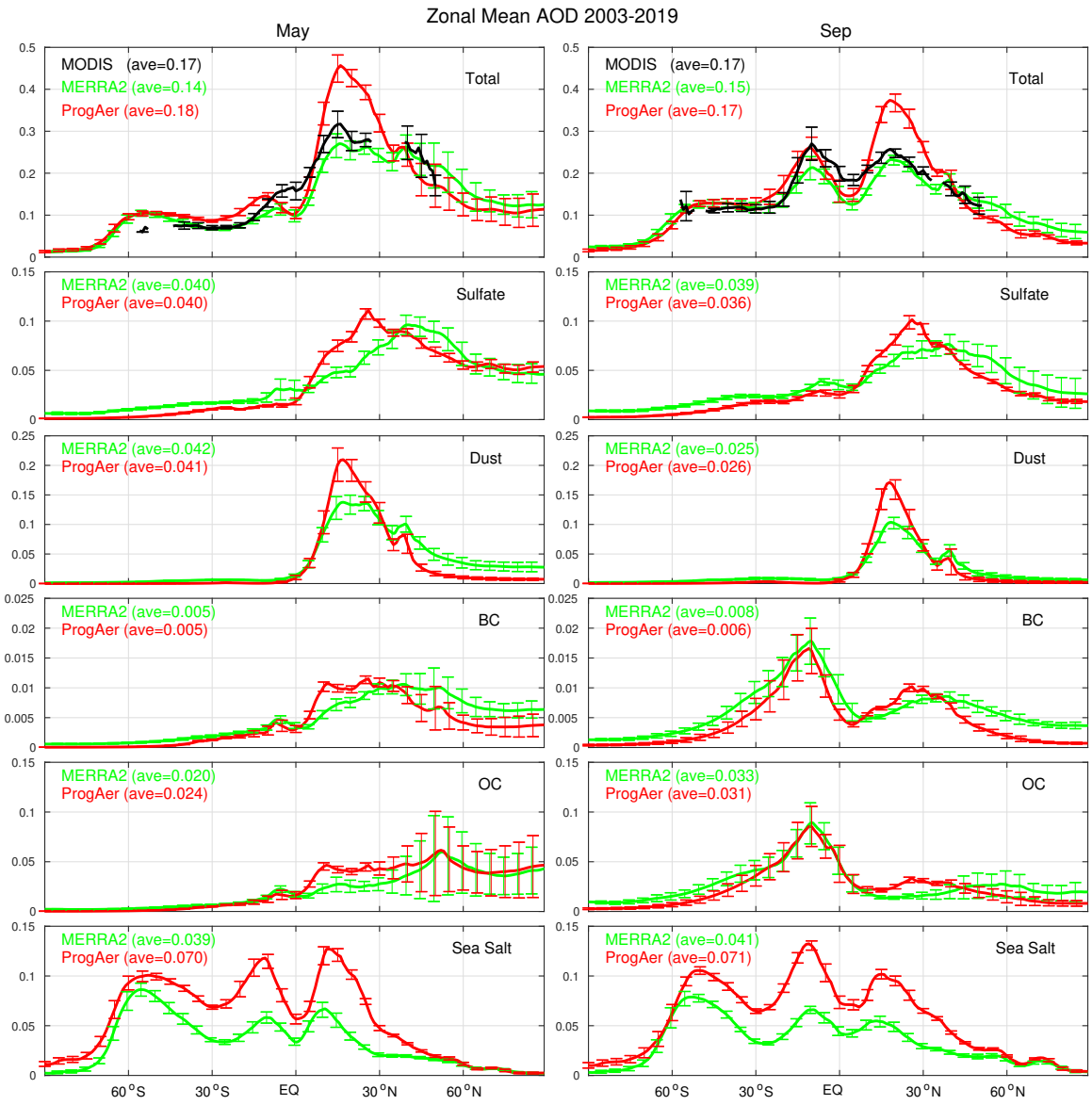

Figure 4. The zonal mean and the standard deviation for total AOD_{550} from MODIS, MERRA2 and Experiment *ProgAer* (top) and its components from sulfate, dust, BC, OC and sea-salt from MERRA2 and Experiment *ProgAer* during 2003-2019 in May (left) and September (right).

Table 3. Five AOD components from Chin et al. (2002) and Experiment *ProgAer* in this study.

AOD	Chin et al. (2002) Year 1990	May/Sep 2003-2009
Dust	0.051	0.041/0.026
Sulfate	0.040	0.040/0.036
Sea salt	0.027	0.070/0.071
OC	0.017	0.024/0.031
BC	0.007	0.005/0.006

iment *ProgAer* show comparable magnitudes for each component, except for the sea-salt AOD, where Experiment *ProgAer* is approximately 2.5 times larger than in Chin et al. (2002). This difference is greater compared to both the MERRA2 and ATom comparisons.

3.2 Radiative Forcing at the Top of the Atmosphere

The radiative forcing at the top of the atmosphere is defined as the difference between the downward and upward radiative flux, expressed as

$$\mathrm{RF}^{\mathrm{TOA}} = \mathrm{Flux}^{\mathrm{TOA}}_{\mathrm{Downward}} - \mathrm{Flux}^{\mathrm{TOA}}_{\mathrm{Upward}}$$

In this fully coupled UFS-CCPP-Chem model, we don't differentiate between RF and effective RF as in IPCC (2013) since both are typically the same and all surface conditions are allowed to adjust. Fig. 6 shows the RF at TOA in the CERES EBAF dataset, as well as the model bias against CERES EBAF for the three experiments mentioned earlier, all based on all-sky conditions. In May and September, the positive bias in RF (positive downward) is predominant in all three experiments, with a global mean ranging from 6 to 7 W/m^2 in Experiments *ProgAer* and *ClimAer* and up to 10 W/m^2 in Experiment *NoAer*. The bias is particularly large along the eastern boundary of the ocean basin off the coast of California, Chile and Angola. Comparison between the experiments with and without aerosols gives an estimate of the total aerosol effects on RF to be about -2.5 W/m^2 globally, which is one order of magnitude bigger than the global mean difference in RF between Experiments *ProgAer* and *ClimAer*. Meanwhile, the bias in RF from the model physics is several times larger than the total aerosol effects on RF.

To further investigate the distribution of the aerosol-radiation effects, we use the equations below

$$\Delta\mathrm{RF}^{\mathrm{TOA}}_{ProgAer} = \mathrm{RF}^{\mathrm{TOA}}_{ProgAer} - \mathrm{RF}^{\mathrm{TOA}}_{NoAer}$$
$$\Delta\mathrm{RF}^{\mathrm{TOA}}_{ClimAer} = \mathrm{RF}^{\mathrm{TOA}}_{ClimAer} - \mathrm{RF}^{\mathrm{TOA}}_{NoAer}$$

to represent the aerosol radiative effects in Experiments *ProgAer* and *ClimAer*, which is defined as the difference in RF from Experiment *NoAer*. The left and middle columns of Fig. 7 show $\Delta\mathrm{RF}^{\mathrm{TOA}}_{ProgAer}$ and $\Delta\mathrm{RF}^{\mathrm{TOA}}_{ClimAer}$ at TOA averaged for May and September over 17 years. The patterns are dominated by the negative flux mostly at low latitudes. The difference between Experiments *ProgAer* and *ClimAer* shown on the right panel of Fig. 7 is much smaller, suggesting the model-simulated RF with prognostic aerosols is similar to that using aerosol climatology on the subseasonal time scale when evaluated over multiple years.

To examine the correlation between $\Delta\mathrm{RF}^{\mathrm{TOA}}_{ProgAer}$ and $\Delta\mathrm{RF}^{\mathrm{TOA}}_{ClimAer}$ with respect to AOD values, we plotted the zonal mean of the left and middle columns in Fig. 7 as

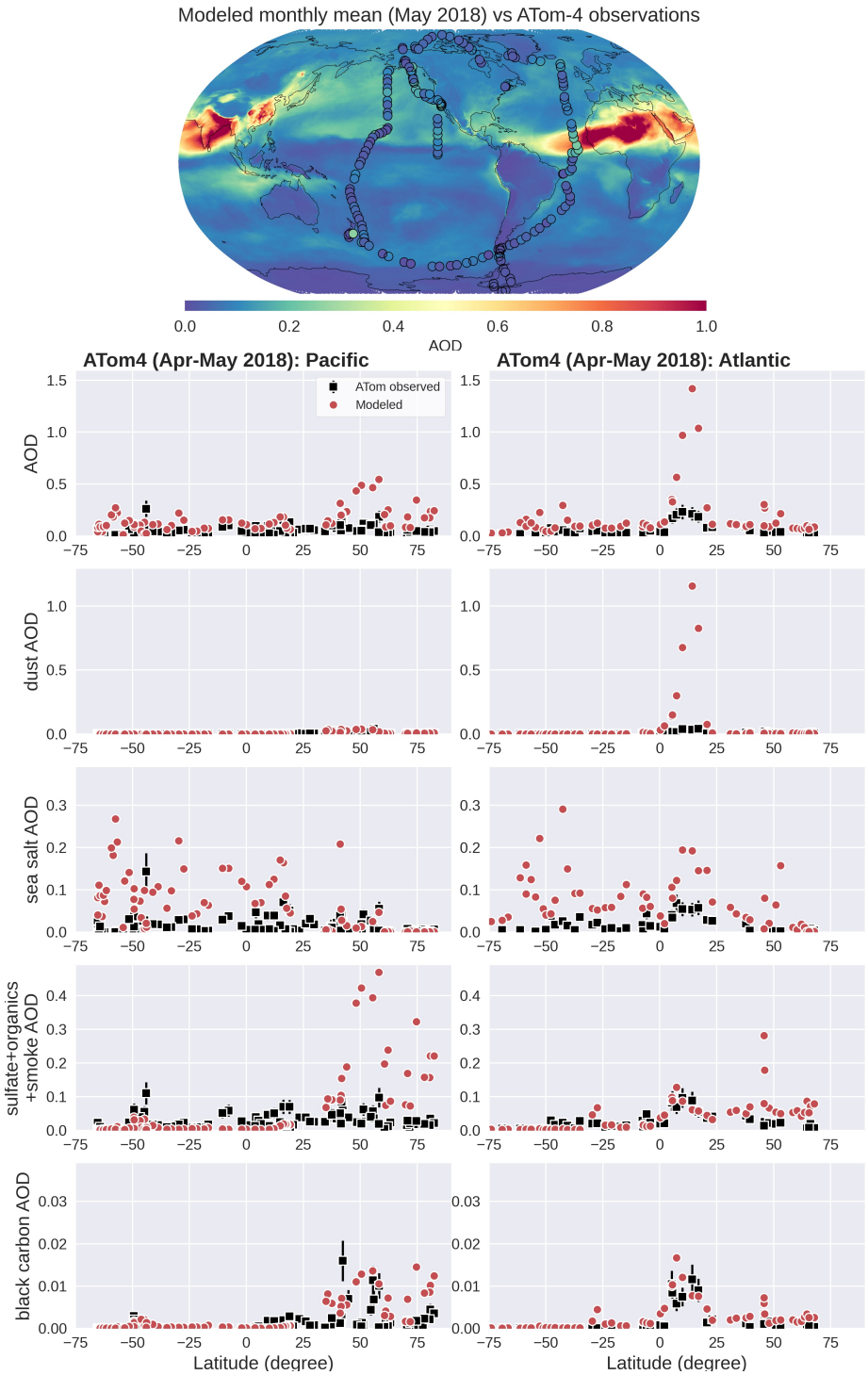

Figure 5. Upper: geographic distribution of the total AOD_{550} from Experiment *ProgAer* overlaying the ATom-4 observations; Lower: modeled AOD (red) shown in the upper panel and its dust, sea-salt, sulfate+OC+smoke and BC components and its comparison to ATom4 (black) in May 2018 in the Pacific (left) and Atlantic (right) section.

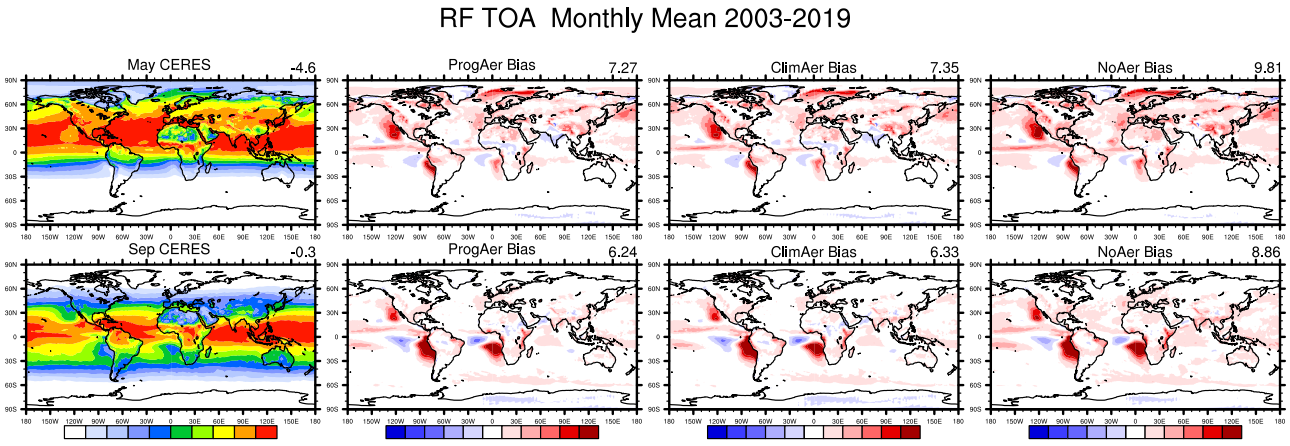

Figure 6. The radiative forcing at TOA (W/m^2, positive downward) in CERES EBAF and biases in Experiments *ProgAer*, *ClimAer* and *NoAer* from CERES EBAF in May (upper) and September (lower) over 17 years.

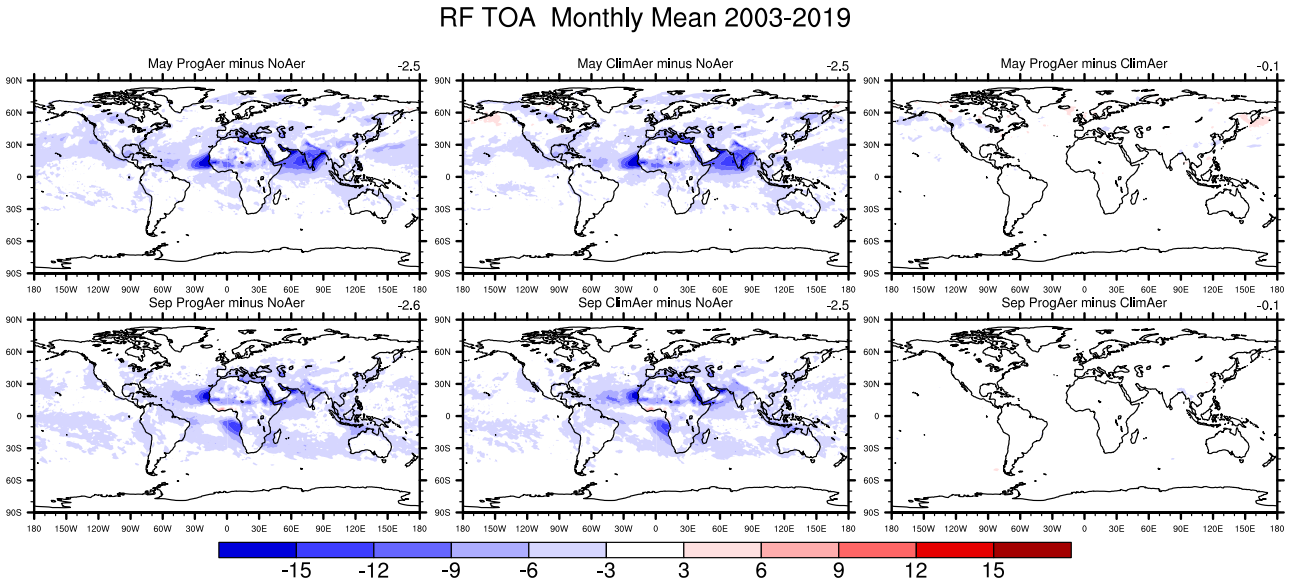

Figure 7. Difference in radiative forcing at TOA (W/m^2, positive downward) of Experiments *ProgAer* (upper) and *ClimAer* (lower) from Experiment *NoAer*, respectively, in May (upper) and September (lower).

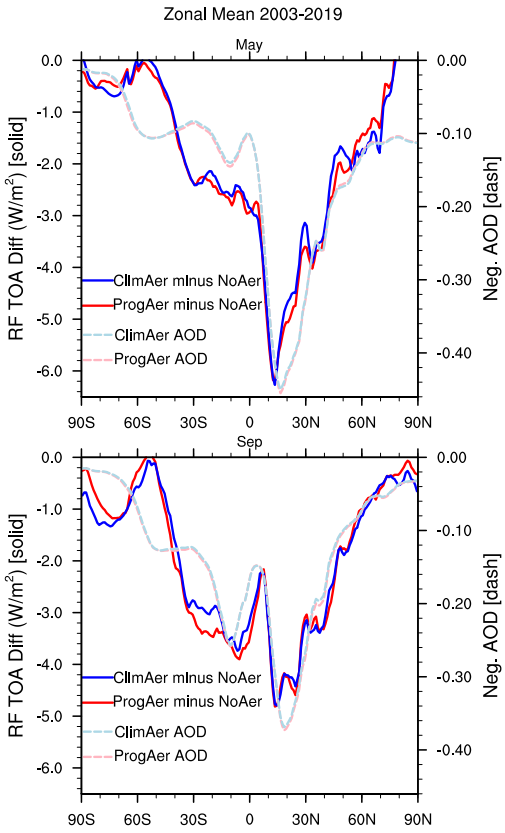

Figure 8. Zonal mean radiative forcing at TOA (W/m^2, positive downward) in Experiments *ProgAer* and *ClimAer* from *NoAer* and their AOD in May (upper) and September (lower). Note that 'negative' AOD is plotted.

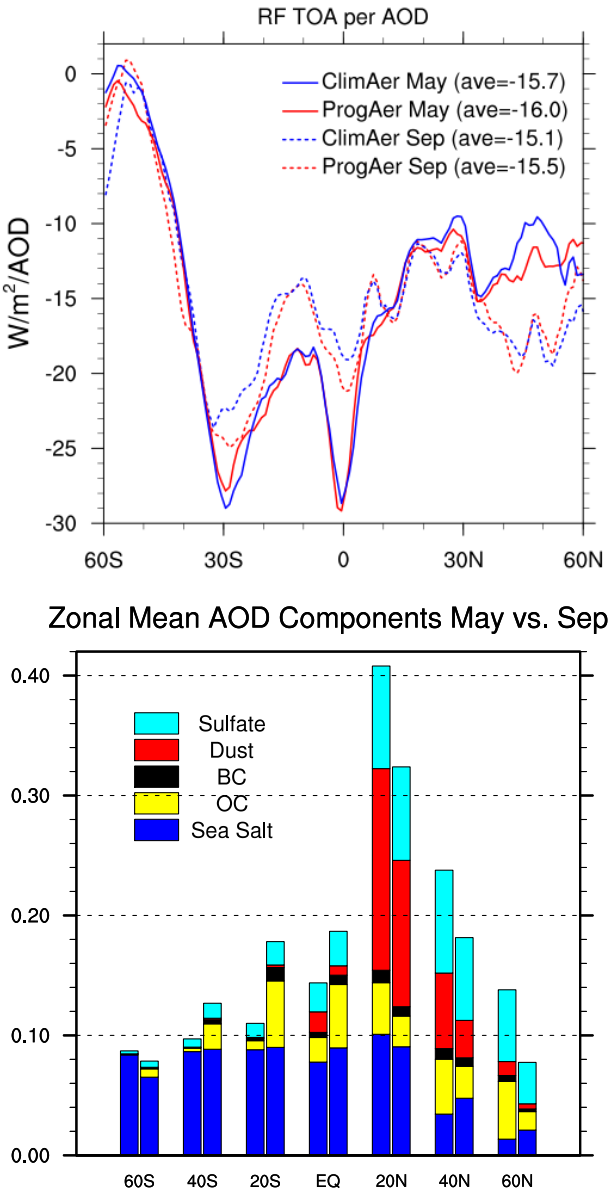

Figure 9. Upper: normalized radiative forcing at TOA per unit AOD, both are zonal mean, from Experiments *ProgAer* and *ClimAer* in May (solid) and September (dashed). Lower: five AOD components in May (left bar) and September (right bar).

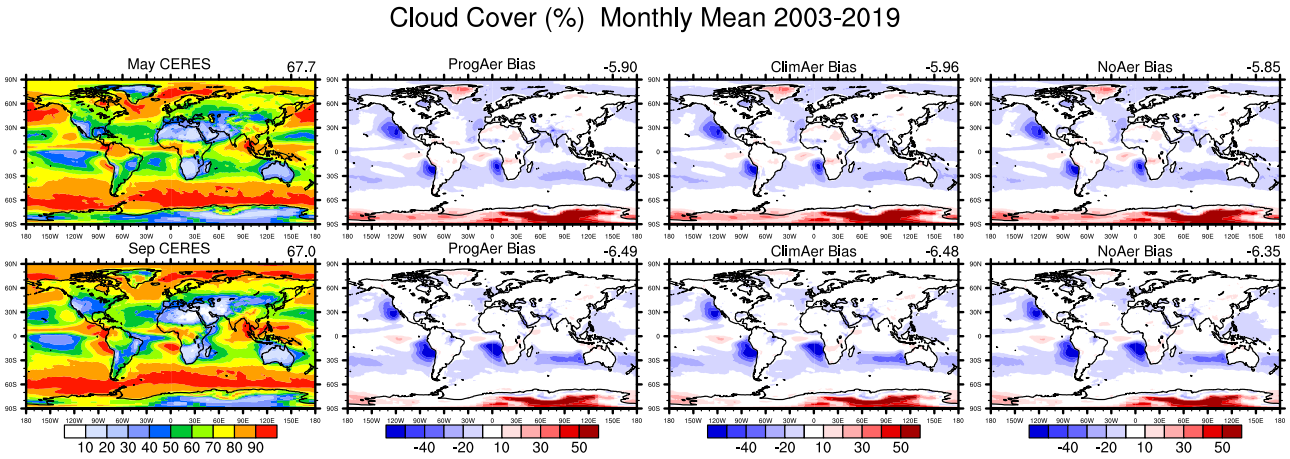

Figure 10. Cloud coverage (%) in CERES EBAF (left) and biases in Experiments *ProgAer*, *ClimAer* and *NoAer* (2nd to 4th column) from CERES EBAF in May (upper) and September (lower).

solid red and blue lines in Fig. 8, respectively, along with the zonal mean 'negative' AOD in dashed lines. The two pairs of curves are well correlated, with the maximum AOD and minimum ΔRF^{TOA} co-located near 15°N, and some discrepancies between the two at certain latitudes. It is worth noting that changes in RF per unit AOD depend on various physical and chemical properties of the aerosols (Bellouin et al., 2020).

To further investigate the efficiency of RF, we calculated the normalized ΔRF^{TOA}, which is the ratio of ΔRF^{TOA} and AOD, both zonal mean, and plotted it in Fig. 9(a) for May and September. The normalized ΔRF^{TOA} between Experiments *ProgAer* and *ClimAer* are very close in magnitude in both months, varying from 0 to -30 W/m^2 per unit AOD, depending on latitudes and seasons. The ratio becomes close to zero south of 45°S, where the sea-salt component dominates. It seems that sea-salt has a relatively lower effect on RF than other components. There are two peak values occurring at the equator and 30°S, with different magnitudes in May and September. The different ratios in season may be related to the time-varying aerosol compositions, as shown in Fig. 9(b), where the magnitude of each AOD component is shown with latitudes for May and September averaged from 2003 to 2019. There are seasonal and latitudinal variabilities in the magnitude of each AOD component between May and September, particularly for OC and dust. These results are consistent with -23.7 ± 3.1 W/m^2 per unit AOD reported in Myhre et al. (2013).

3.3 Cloud Coverage

Fig. 10 shows the total cloud coverage from the CERES EBAF dataset as the 'truth', along with the biases in modeled cloud cover from three experiments: *ProgAer*, *ClimAer* and *NoAer*. All products are monthly averages in May and September from 2003 to 2019. The global mean cloud coverage in May and September in the CERES EBAF is 67.7% and 67.0%, respectively. The modeled cloud coverage from all three model experiments has a similar negative bias, ranging from -6.0% to -5.8% globally in May and from -6.5% to -6.3% in September. The bias pattern in clouds is similar to that in RF at TOA shown

in Fig. 6, where the lack of clouds along the east boundary of ocean basins off the continents explains the lack of upward radiation at TOA.

There is little difference in cloud coverage among the three experiments featuring different aerosols, whereas the variance in RF at TOA can reach up to -2.5 W/m^2. This suggests that the alteration in cloud coverage due to aerosol-radiation interaction, known as the semi-direct effect, remains negligible regardless of whether the aerosols are prognosed, based on climatology, or even absent. This is expected given that this version of the model employs a single-moment microphysics parameterization.

It is worth noting that a model bias of approximately 6% in cloud coverage leads to a bias of about +12 W/m^2 in RF in May and +6 W/m^2 in September, which is several times larger than the estimated aerosol effects on RF of -2.5 W/m^2. Evidently, clouds have a more substantial impact on RF than aerosols, although the significance of aerosols should not be overlooked.

3.4 Hemispheric Surface Temperature, H500 and Precipitation

With the analysis of radiative forcing and cloud coverage associated with different aerosols in Experiments *NoAer*, *ClimAer* and *ProgAer* shown above, we investigate the impact of aerosols on meteorological fields across these three experiments. Fig. 11 presents the anomaly correlation coefficient (ACC) for the predicted surface temperature at 2 m (T2m) and H500 against ERA5 reanalysis, and precipitation against GPCP data. The analysis covers the 20°N-80°N (NHX) and 20°S-80°S (SHX) regions, with lead times ranging from weeks 1 to 4 and a combination of weeks 3 and 4, in May and September from 2003 to 2019. At weeks 1 and 2, the ACC scores for T2m, H500 and precipitation remain consistent across the experiments, irrespective of the variations in aerosol loadings. This pattern holds true for both May and September initializations, suggesting that the ACC scores at these lead times are minimally influenced by aerosol levels on a hemispheric scale. At longer lead times of weeks 3+4 in the SHX, Experiment *ProgAer* shows the highest ACC values for both T2m and H500 in May but the lowest in September. Meanwhile, in the NHX, the ACC scores for T2m and H500 are similar.

In these experiments, precipitation is not influenced by aerosol-cloud interactions, as they are not parameterized. Instead, the impact of aerosols on precipitation primarily comes from the thermodynamic fields, which have a minimal effect. The precipitation skill beyond week 2 is low and no longer significant.

The results presented suggest a number of implications. First, despite the well-understood and accurately simulated radiative forcing from the aerosol-radiation interaction within the model, its significant influence on surface temperature and H500 is not evident in these experiments. Second, the discrepancies in the ACC values from Experiment *ProgAer* across different hemispheres could be attributed to the accuracy of prescribed emission sources and parameterized emission sinks, especially in the SHX during September. Additionally, the parameterization of aerosol-cloud interaction appears to be crucial in capturing the impact of aerosols on precipitation patterns.

3.5 Aerosol Regional Impact

As shown in the Figs 7 and 8, the modeled RF differences of Experiments *ProgAer* and *ClimAer* from *NoAer* ($\Delta\mathrm{RF}^{\mathrm{TOA}}_{ProgAer}$ and $\Delta\mathrm{RF}^{\mathrm{TOA}}_{ClimAer}$) shows similarities when assessed as averages over 17 years. However, there are significant interannual variabilities in AOD and its associated RF in regions such as Sahara. For instance, the AOD over northern Africa in Experiment *ProgAer* exceeds that in Experiment *ClimAer* by 0.15 in May 2004, according to Fig. 3(c). As an example, we chose a domain over northern Africa larger than the one used in Fig. 3 to show the horizontal distribution of AOD, net radiative forcing at TOA and surface, as well as T2m in May 2004 in Experiment

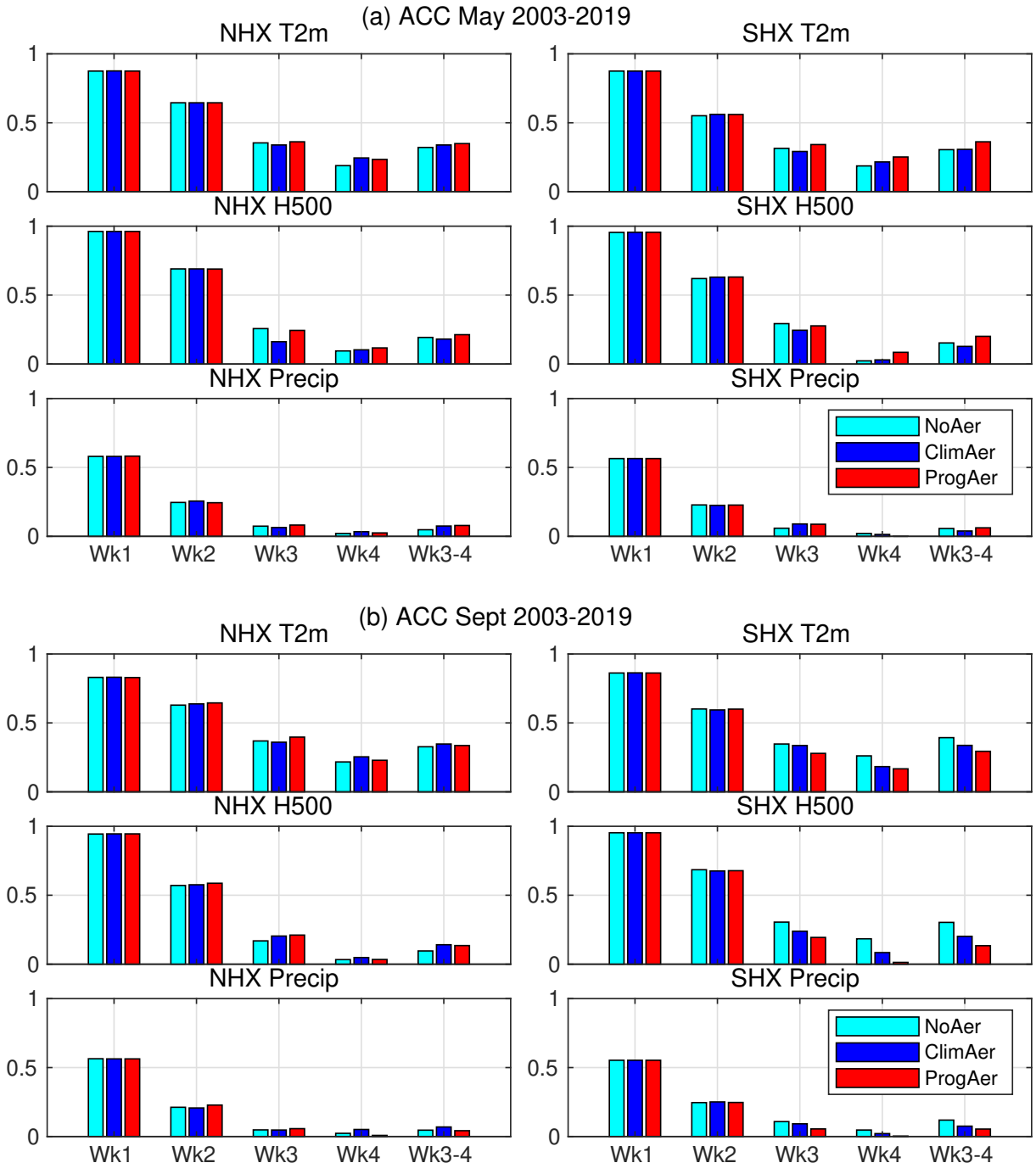

Figure 11. Anomaly correlation coefficient for T2m, H500 and precipitation at different lead times from Experiments *ProgAer*, *ClimAer* and *NoAer*, from 2003 to 2019, in May (a) and September (b), for northern hemisphere (left) and southern hemisphere (right).

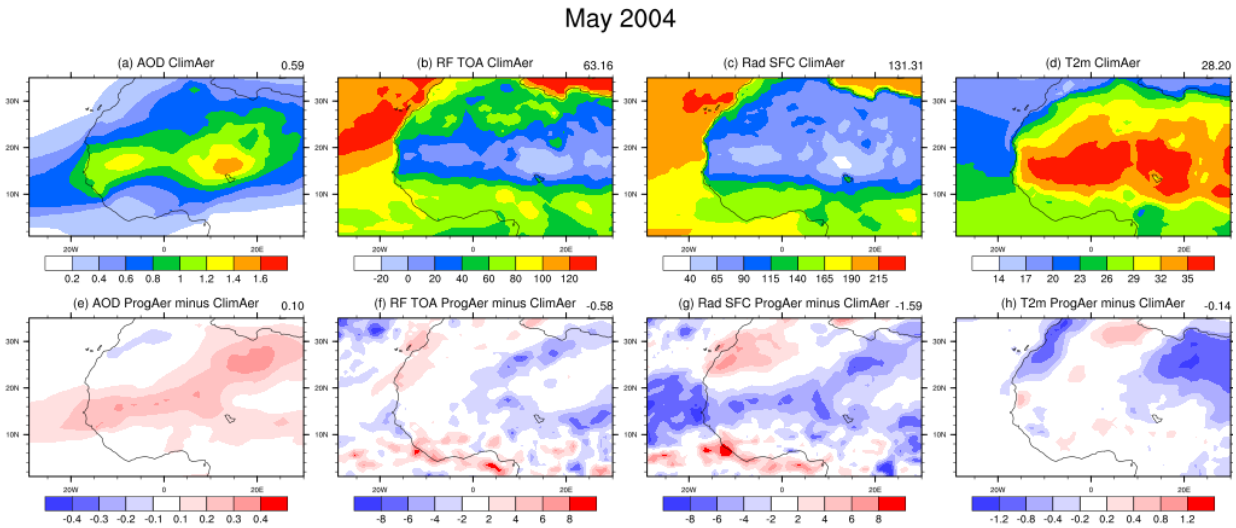

Figure 12. From left to right: AOD, radiative forcing at TOA and surface (W/m^2), and T2m (°C) in Experiment *ClimAer* (upper) and the difference of Experiments *ProgAer* and *ClimAer* (lower), all monthly means in May 2004. Numbers in the upper-right corner are the means over the displayed domain. Positive values are downward for fluxes.

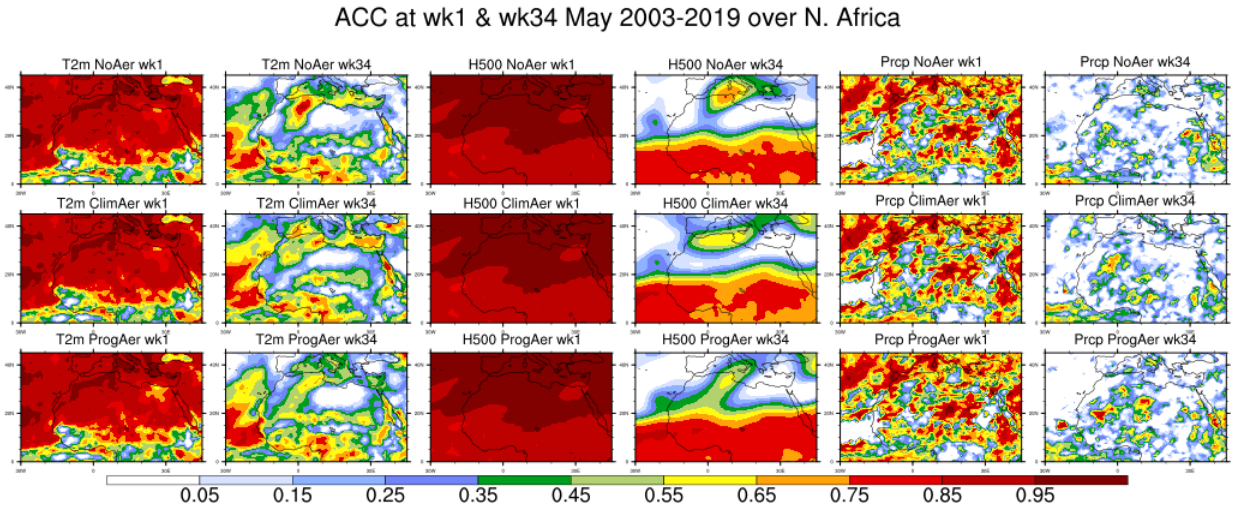

Figure 13. ACC at lead time of week 1 and weeks 3 and 4 combined of T2m (leftmost two columns), H500 (third and fourth columns) and precipitation (rightmost two columns) over northern Africa for Experiments *NoAer* (top), *ClimAer* (middle) and *ProgAer* (bottom). All model experiments are initialized on the first of May, 2003-2019.

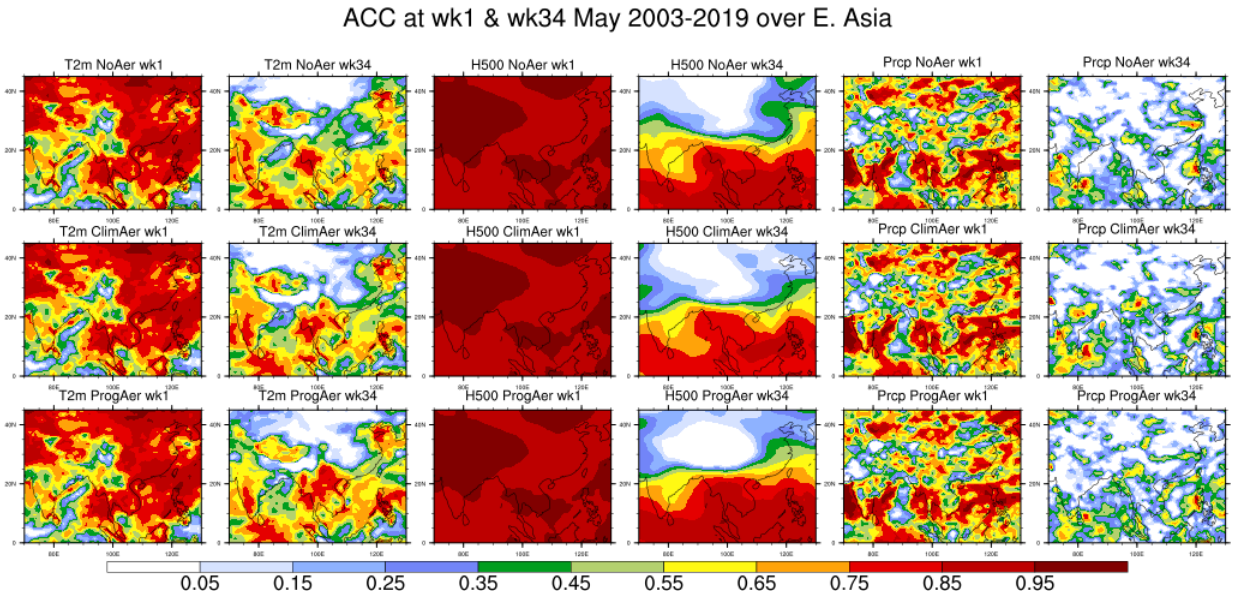

Figure 14. Same as Fig. 13, except for east Asia.

ClimAer when aerosol climatology is used in the upper row of Fig. 12. The impact of prognostic aerosols on these fields are shown as difference of Experiments *ProgAer* and *ClimAer* in the lower row of Fig. 12. The AOD in Experiment *ProgAer* exceeds the one from the aerosol climatology run, mostly over the Sahara and Sahel regions as shown in Fig. 12(e). A negative RF at TOA and surface is shown in the same regions in Fig. 12(f) and (g) as expected. Noteworthy correlations exist in the difference patterns between AOD and RF at TOA in Fig. 12(e) and (f), as well as between AOD and RF at the surface in Fig. 12(e) and (g). This suggests that the aerosol-radiation interaction and its variations with different aerosol loadings are well-captured in this episode over northern Africa. However, there is no apparent correlation in the difference patterns between AOD and surface temperature in Fig. 12(e) and (h), similar to what is discussed in Sec. 3.4.

To further investigate the regional effects of aerosols on meteorological patterns, Fig. 13 shows the ACC scores for T2m (leftmost two columns), H500 (third and fourth columns) and precipitation (rightmost two columns), at lead times of week 1 and weeks 3+4 in May from 2003 to 2019 over northern Africa. Despite large variations in aerosol loadings used in these simulations, as indicated in Fig. 3, the ACC scores for T2m, H500 and precipitation are remarkably similar at week 1 among the three experiments. In the subsequent weeks 3+4, Experiment *ProgAer* shows marginally higher ACC scores for T2m and H500 in the Sahel region and adjacent to the Africa coast, yet these scores are reduced over northern Africa when compared to the other two experiments. As anticipated, the ACC for precipitation remains notably low during weeks 3+4.

East Asia, a region characterized by relatively high aerosol concentrations, as shown in Fig. 3. Fig. 14, is examined for its meteorological response. Fig. 14 shows the ACC scores for T2m, H500 and precipitation for this region in May, presented in a similar manner to Fig. 13. Consistency in the ACC scores at week-1 across the three experiments indicates a minimal influence of aerosol concentrations on these metrics at this lead time. However, during the weeks 3+4 period, Experiment *ProgAer* shows elevated ACC scores for T2m and H500 in Southeast Asia, while these scores are diminished over Central Asia when compared to the other experiments.

Figs. 13 and 14 reveal modest regional variations in skill for T2m and H500 within the prognostic aerosol experiments over a lead time of weeks 3+4. These findings are based on a limited set of experiments conducted from 2003 to 2019.

4 Summary and Conclusion

This study investigates the aerosol radiative effects on subseasonal prediction using the UFS-CCPP-Chem, the Unified Forecast System integrated with a CCPP-based aerosol module from the GEFS-Aerosols model. We evaluated the top-of-the-atmosphere radiative forcing from tropospheric aerosols, including sulfate, dust, black carbon, organic carbon, and sea-salt. Our research involved three sets of UFS-CCPP-Chem simulations: *ProgAer*, featuring an interactive aerosol module, *ClimAer*, which applies aerosol climatology derived from Experiment *ProgAer* in place of the interactive aerosol module, and *NoAer*, which excludes aerosol effects. We used monthly mean estimates, including zonal or global average, for model evaluation, despite the recognized spatial and temporal heterogeneity of aerosol distributions.

Our analysis, based on experiments initialized on May 1 and September 1 from 2003 to 2019, reveals that the monthly mean AOD patterns and interannual variability from Experiment *ProgAer* align well with MODIS satellite observations, MERRA2 reanalysis, and ATom-4 aircraft observations, despite some discrepancies between these datasets. Model simulations reveal a positive bias in dust AOD over the Sahara and sea-salt AOD across most oceans, possibly due to biases in the aerosol module. Furthermore, modeled cloud coverage is less than that in the CERES EBAF dataset, likely from inadequate model physics parameterization, contributing to inaccuracies in the radiation.

To correct for model bias, we compared the radiative forcing at the top-of-atmosphere between Experiment *ProgAer* and *NoAer*, using this as an indicator of the total aerosol radiative forcing. Our calculations suggest a global average of approximately -2.5 W/m^2 at the TOA. This figure aligns with findings from prior research, such as the -1.0 W/m^2 in IPCC (2013) and -1.2 W/m^2 in Bellouin et al. (2020), which focus solely on the anthropogenic component of radiative forcing since the pre-industrial era. In contrast, our model's estimate includes both anthropogenic and natural aerosol sources. Additionally, we determined the normalized radiative forcing to be approximately -16 W/m^2 per unit AOD globally.

Contrary to expectations, incorporating aerosol-radiation interaction into the model simulations does not consistently improve the forecast skill for T2m and H500. The ACC for these variables at a 1-week lead time remains comparable across various aerosol scenarios. With increasing lead times, the forecast outcomes become mixed, suggesting that the predictive accuracy for T2m and H500 is affected by the intricate relationship between aerosols and meteorology. This variation in forecast skill over extended lead times highlights the complexity of the aerosol-meteorology interaction and emphasizes the importance of careful consideration of both aerosol-radiation and aerosol-cloud interactions, along with addressing biases in model physics for long-range forecasts and the accuracy in aerosol emission datasets.

Moreover, the impact of aerosols on cloud formation and precipitation through radiative processes is not readily apparent due to the single-moment microphysics parameterization employed in this version of the model. In the UFS-CCPP-Chem experiments, despite a global RF difference of approximately -2.5 W/m^2 at the TOA with and without aerosol-radiation interaction, cloud coverage and precipitation patterns remain largely unchanged. This indicates that the modeled semi-direct effects of aerosol-radiation interaction on cloudiness and precipitation are minimal. Current efforts are focused on simulating the indirect effects using a double-moment microphysics parameterization in the upcoming version of the UFS.

This study represents one of the initial efforts to evaluate the aerosol radiation effects on subseasonal forecasts using the UFS. Notably, local regions exhibited significant radiative forcing discrepancies, particularly where the AOD differences between prognosed and climatological aerosols were exceptionally pronounced during certain events. The UFS-CCPP-Chem, utilizing modeled climatological aerosol concentrations, successfully captures the average radiative forcing seen in simulations with prognosed aerosols over subseasonal timescales, albeit without the interannual aerosol variabilities. Nevertheless, given the current constraints within this aerosol module, including demonstrated biases and uncertainties in time-varying aerosol emission datasets, the potential benefits of utilizing a prognostic aerosol module are limited. This prompts consideration for substituting the resource-intensive chemistry module with an aerosol climatology in subseasonal applications. Additionally, the development of a global, high-quality, and high-resolution aerosol climatology, derived from either observations or reanalysis, is essential to mitigate uncertainties inherent in aerosol modeling.

Open Research Section

The model data from three sets of experiments used in this study, as well as the NCL and MATLAB scripts used to produce the figures, are available on GitHub at `https://github.com/ShanSunNOAA/WGNE_2024`. The MODIS dataset and MERRA2 reanalysis are available at Bhattacharjee et al. (2023). The aerosol dataset from ATom including AOD is available at Brock et al. (2021).

Acknowledgments

This research is supported by the base funds from the NOAA Global Systems Laboratory. LZ, SW, DH and HL are supported by NOAA cooperative agreements NA17OAR4320101 and NA22OAR4320151. We thank the EMC group and the associated community for their multiyear effort of developing and improving the UFS model. The constructive suggestions from Dr. Dave Turner during the interval review is much appreciated. The authors acknowledge the NOAA Research and Development High Performance Computing Program for providing computing and storage resources.

References

Ahmadov, R., Grell, G., James, E., Csiszar, I., Tsidulko, M., Pierce, B., ... Goldberg, M. (2017). *Using viirs fire radiative power data to simulate biomass burning emissions, plume rise and smoke transport in a real-time air quality modeling system.* Ieee International Geoscience and Remote Sensing Symposium, IEEE International Geoscience and Remote Sensing Symposium (IGARSS). Retrieved from `https://doi.org/10.1109/IGARSS.2017.8127581`

Baklanov, A., Schlünzen, K., Suppan, P., Baldasano, J., Brunner, D., Aksoyoglu, S., ... Zhang, Y. (2014). Online coupled regional meteorology chemistry models in europe: current status and prospects. *Atmos. Chem. Phys.*, *14*, 317-398.

Bellouin, N., Quaas, J., Gryspeerdt, E., Kinne, S., Stier, P., Watson-Parris, D., ... Stevens, B. (2020). Bounding global aerosol radiative forcing of climate change. *Reviews of Geophysics*, *8*, e2019RG000660. Retrieved from `https://doi.org/10.1029/2019RG000660`

Benedetti, A., & Vitart, F. (2018). Can the direct effect of aerosols improve subseasonal predictability? *Mon. Wea. Rev.*, *146*, 3481-3498.

Bhattacharjee, P. S., Zhang, L., Baker, B., Pan, L., Montuoro, R., Grell, G. A., & McQueen, J. T. (2023). *Evaluation of aerosol optical depth forecasts from noaa's global aerosol forecast model (gefs-aerosols)* (Vol. 38) (No. 2). Retrieved

from https://doi.org/10.1175/waf-d-22-0083.1

Brock, C. A., Froyd, K. D., Dollner, M., Williamson, C. J., Schill, G., Murphy, D. M., ... Wofsy, S. C. (2021). Ambient aerosol properties in the remote atmosphere from global-scale in situ measurements. *Atmos. Chem. Phys.*, *21*, 15023–15063. Retrieved from https://doi.org/10.5194/acp-21-15023-2021

Buchard, V., Randles, C. A., da Silva, A. M., Darmenov, A., Colarco, P. R., Govindaraju, R., ... Yu, H. (2017). The merra-2 aerosol reanalysis, 1980-onward, part ii: Evaluation and case studies. *J. Climate*, *30*, 6851-6872. Retrieved from https://doi.org/10.1175/JCLI-D-16-0613.1

Carslaw, K. S., Lee, L. A., Reddington, C. L., Pringle, K. J., Rap, A., Forster, P. M., ... Pierce, J. R. (2013). Large contribution of natural aerosols to uncertainty in indirect forcing. *Nature*, *503*, 67–71. Retrieved from https://doi.org/10.1038/nature12674

Chin, M., Ginoux, P., Kinne, S., Torres, O., Holben, B. N., Duncan, B. N., ... Nakajima, T. (2002). Tropospheric aerosol optical thickness from the gocart model and comparisons with satellite and sun photometer measurements. *J. Atmos. Sci.*, *59*, 461-483.

Chin, M., Rood, R. B., Lin, S.-J., Müller, J.-F., & Thompson, A. M. (2000). Atmospheric sulfur cycle in the global model gocart: Model description and global properties. *J. Geophys. Res.*, *105*(24), 24,661-24,687.

Colarco, P., da Silva, A., Chin, M., & Diehl, T. (2010). Online simulations of global aerosol distributions in the nasa geos-4 model and comparisons to satellite and ground-based aerosol optical depth. *J. Geophys. Res.*, *115*, D14207. Retrieved from https://doi:10.1029/2009JD012820

Fast, J., Jr., W. G., Easter, R., Zaveri, R., Barnard, J., Chapman, E., ... Peckham, S. (2006). Evolution of ozone, particulates, and aerosol direct forcing in an urban area using a new fully-coupled meteorology, chemistry, and aerosol model. *J. Geophys. Res.*, *111*(5), D21305.

Frassoni, A., Benedettio, A., Vitarto, F., & Engelbrecht, F. (2021). *The second phase of the wgne aerosol project: Evaluating aerosol impacts on numerical weather and subseasonal prediction.* Retrieved from https://wgne.net/bluebook/uploads/2019/docs/07_Frassoni_Ariane_The_Second_Phase_of_the_WGNE_Aerosol_Project.pdf

Freitas, S., da Silva, A., Benedetti, A., Grell, G., Jorba, O., & Mokhtari, M. (2015). *Evaluating aerosol impacts on numerical weather prediction: A wgne initiative.* Symposium on Coupled Chemistry-Meteorology/Climate Modeling, Switzerland.

Freitas, S. R., Longo, K. M., Chatfield, R., Latham, D., Silva Dias, M. A. F., Andreae, M. O., ... Carvalho Jr., J. A. (2007). Including the sub-grid scale plume rise of vegetation fires in low resolution atmospheric transport models. *Atmos. Chem. Phys.*, *7*, 3385–3398. Retrieved from https://doi.org/10.5194/acp-7-3385-2007

Grell, G. A., & Baklanov, A. (2011). Integrated modeling for forecasting weather and air quality: A call for fully coupled approaches. *Atmos. Environ.*, *45*, 6845–6851.

Grell, G. A., Freitas, S. R., Stuefer, M., & Fast, J. D. (2011). Inclusion of biomass burning in wrf-chem: Impact of wildfires on weather forecasts. *Atmos. Chem. Phys.*, *11*, 1–16. Retrieved from https://doi:10.5194/acp-11-1-2011

Grell, G. A., Peckham, S. E., Schmitz, R., McKeen, S. A., Frost, G., Skamarock, W. C., & Eder, B. (2005). Fully coupled "online" chemistry within the wrf model. *Atmos. Environ.*, *39*, 6957–6975.

Hansen, J., Lacis, A., Ruedy, R., & Sato, M. (1992). Potential climate impact of mount pinatubo eruption. *Geophys. Res. Lett.*, *19*, 215–218. Retrieved from https://doi.org/10.1029/91GL02788

Harris, L., Chen, X., Putman, W., Zhou, L., & Chen, J. H. (2021). *A scientific description of the gfdl finite-volume cubed-sphere dynamical core.* NOAA technical memorandum OAR GFDL. Retrieved from https://doi.org/10.25923/6nhs-5897

Haustein, K., Pèrez, C., Baldasano, J. M., Jorba, O., Basart, S., Miller, R. L., ... Schladitz, A. (2012). Atmospheric dust modeling from meso to global scales with the online nmmb/bsc-dust model – part 2: Experimental campaigns in northern africa. *Atmos. Chem. Phys.*, *12*, 2933–2958. Retrieved from https://doi.org/10.5194/acp-12-2933-2012

Haywood, J. M., Allan, R. P., Culverwell, I., Slingo, T., Milton, S., Edwards, J., & Clerbaux, N. (2005). Can desert dust explain the outgoing longwave radiation anomaly over the sahara during july 2003? *J. Geophys. Res.*, *110*, D05105.

Heinzeller, D., Bernardet, L., Firl, G., Zhang, M., Sun, X., & Ek, M. (2023). The common community physics package (ccpp) framework v6. *Geosci. Model Dev.*, *16*, 2235-2259. Retrieved from https://doi.org/10.5194/gmd-16-2235-2023

Hersbach, H., Bell, B., Serrisford, P., Hirahara, S., Horànyi, A., noz Sabater, J. M., ... co authors (2020). The era5 global reanalysis. *Quarterly Journal of the Royal Meteorological Society*, *146*, 1999-2049. Retrieved from https://doi.org/10.1002/qj.3803

Hoesly, R. M., Smith, S. J., Feng, L., Klimont, Z., Janssens-Maenhout, G., Pitkanen, T., ... Zhang, Q. (2018). Historical (1750–2014) anthropogenic emissions of reactive gases and aerosols from the community emissions data system (ceds). *Geosci. Model Dev.*, *11*, 369–408.

Huffman, G. J., Adler, R. F., Morrissey, M. M., Bolvin, D. T., Curtis, S., Joyce, R., ... Susskind, J. (2001). Global precipitation at one-degree daily resolution from multisatellite observations. *J. Hydrometeor.*, *2*(1), 36-50.

Hunke, E. C., Lipscomb, W. H., Turner, A. K., Jeffery, N., & Elliott, S. (2015). *Cice: the los alamos sea ice model documentation and software user's manual version 5.1.* Los Alamos Natl. Lab., Los Alamos, N. M.

IPCC. (2013). *Climate change 2013: The physical science basis. contribution of working group i to the fifth assessment report of the intergovernmental panel on climate change [stocker, t.f., d. qin, g.-k. plattner, m. tignor, s.k. allen, j. boschung, a. nauels, y. xia, v. bex and p.m. midgley (eds.)].* Cambridge University Press, Cambridge, United Kingdom and New York, NY, USA. doi: doi:10.1017/CBO9781107415324

IPCC. (2021). *Summary for policymakers. in: Climate change 2021: The physical science basis.* Contribution of Working Group I to the Sixth Assessment Report of the Intergovernmental Panel on Climate Change [Masson-Delmotte, V., P. Zhai, A. Pirani, S. L. Connors, C. Péan, S. Berger, N. Caud, Y. Chen, L. Goldfarb, M. I. Gomis, M. Huang, K. Leitzell, E. Lonnoy, J.B.R. Matthews, T. K. Maycock, T. Waterfield, O. Yelekçi, R. Yu and B. Zhou (eds.)]. Cambridge University Press. In Press.

Kaiser, J., Heil, A., Andreae, M., Benedetti, A., Chubarova, N., Jones, L., ... van der Werf, G. (2012). Biomass burning emissions estimated with a global fire assimilation system based on observed fire radiative power. *Biogeosciences*, *9*, 527–554.

Le Treut, H., Forichon, M., Boucher, O., & Li, Z. (1998). Sulfate aerosol indirect effect and co2 greenhouse forcing: Equilibrium response of the lmd gcm and associated cloud feedbacks. *J. Climate*, *11*(7), 1673-1684.

Levy, R. C., Mattoo, S., Munchak, L. A., Remer, L. A., Sayer, A. M., Patadia, F., & Hsu, N. (2013). The collection 6 modis aerosol products over land and ocean. *Atmos. Meas. Tech.*, *6*, 2989–3034. Retrieved from https://doi.org/10.5194/amt-6-2989-2013

Liu, Y., Wang, W., Kumar, A., & Collow, T. (2019). *Assessment of cpc sea ice*

initialization system (csis) and cpc weekly experimental sea ice forecasts. 44th NOAA Annual Climate Diagnostics and Prediction Workshop. Retrieved from https://www.nws.noaa.gov/ost/climate/STIP/44CDPW/44cdpw-YLiu.pdf

Loeb, N. G., Doelling, D. R., Wang, H., Su, W., Nguyen, C., Corbett, J. G., ... Kato, S. (2018). Clouds and the earth's radiant energy system (ceres) energy balanced and filled (ebaf) top-of-atmosphere (toa) edition-4.0 data product. *J. Climate*, *31*(2), 895–918. Retrieved from https://doi.org/10.1175/JCLI-D-17-0208.1

Madden, R. A., & Julian, P. R. (1971). Detection of a 40–50 day oscillation in the zonal wind in the tropical pacific. *J. Atmos. Sci.*, *28*, 702–708. Retrieved from https://doi.org/10.1175/1520-0469(1971)028<0702:DOADOI>2.0.CO;2

Mann, G. W., Carslaw, K. S., Reddington, C. L., Pringle, K. J., Schulz, M., Asmi, A., ... Henzing, J. S. (2014). Intercomparison and evaluation of global aerosol microphysical properties among aerocom models of a range of complexity. *Atmos. Chem. Phys.*, *14*(9), 4679-4713. Retrieved from https://acp.copernicus.org/articles/14/4679/2014/

Ming, Y., Ramaswamy, V., Ginoux, P. A., & Horowitz, L. H. (2005). Direct radiative forcing of anthropogenic organic aerosol. *J. Geophys. Res.-Atmos.*, *110*, D20208. Retrieved from doi.org/10.1029/2004JD005573

Mitchell, J. M. (1971). The effect of atmospheric aerosols on climate with special reference to temperature near the earth's surface. *J. of Applied Meteorology*, 703-714.

Mitchell, K. (2005). *The community noah land-surface model (lsm) user's guide, public release version 2.7.1.* Retrieved from https://ral.ucar.edu/sites/default/files/public/product-tool/unified-noah-lsm/Noah_LSM_USERGUIDE_2.7.1.pdf

Mulcahy, J. P., Walters, D. N., Bellouin, N., & Milton, S. F. (2014). Impacts of increasing the aerosol complexity in the met office global numerical weather prediction model. *Atmos. Chem. Phys.*, *14*(9), 4749-4778. Retrieved from doi:10.5194/acp-14-4749-2014

Murakami, H. (2022). Substantial global influence of anthropogenic aerosols on tropical cyclones over the past 40 years. *Sci Adv.*, *8*(19). doi: 10.1126/sciadv.abn9493

Myhre, G., Samset, B. H., Schulz, M., Balkanski, Y., Bauer, S., & Berntsen, T. K. e. a. (2013). Radiative forcing of the direct aerosol effect from aerocom phase ii simulations. *Atmos. Chem. Phys.*, *13*, 1853–1877. Retrieved from https://doi.org/10.5194/acp-13-1853-2013

NOAA. (2021). *Upgrade ncep global forecast systems (gfs) to v16: Effective march 17, 2021.* Service Change Notice 21-20, Updated. National Weather Service Headquarters, Silver Spring MD, https://www.weather.gov/media/notification/scn_21-20_gfsv16.0_aaa_update.pdf.

Pan, B., Wang, Y., Logan, T., Hsieh, J., Jiang, J. H., Li, Y., & Zhang, R. (2020). Determinant role of aerosols from industrial sources in hurricane harvey's catastrophe. *Geophysical Research Letters*, *47*, e2020GL090014. Retrieved from https://doi.org/10.1029/2020GL090014

Pérez, C., Nickovic, S., Pejanovic, G., Baldasano, J. M., & Özsoy, E. (2006). Interactive dust-radiation modeling: A step to improve weather forecasts. *J. Geophys. Res.*, *111*, D16206. Retrieved from https://doi.org/10.1029/2005JD006717

Reale, O., Lau, K. M., & da Silva, A. (2011). Impact of interactive aerosol on the african easterly jet in the nasa geos-5 global forecasting system. *Weather and Forecasting*, *26*, 504-519.

Reale, O., Lau, K. M., da Silva, A., & Matsui, T. (2014). Impact of assimilated and interactive aerosol on tropical cyclogenesis. *Geophys. Res. Lett.*, *41*, 3282–3288. Retrieved from https://doi.org/10.1002/2014GL059918

Reddington, C. L., Carslaw, K. S., Stier, P., Schutgens, N., Coe, H., Liu, D., ... Zhang, Q. (2017). The global aerosol synthesis and science project (gassp): measurements and modeling to reduce uncertainty. *BAMS*, 1857-1877.

Reid, J., Benedetti, A., Colarco, P., & Hansen, J. (2011). International operational aerosol observability workshop. *BAMS*, *92*, ES21-ES24. Retrieved from https://doi.org/10.1175/2010BAMS3183.1

Rodwell, M., & Jung, T. (2008). Understanding the local and global impacts of model physics changes: an aerosol example. *Q J ROY METEOR SOC*, *134*(635), 1479–1497.

Saha, S., Moorthi, S., Pan, H.-L., Wu, X., Wang, J., Nadiga, S., ... Goldberg, M. (2010). Ncep climate forecast system reanalysis. *Bulletin of the American Meteorological Society*, *91*, 1015-1058.

Saide, P. E., Spak, S. N., Pierce, R. B., Otkin, J. A., Schaack, T. K., Heidinger, A. K., ... Carmichael, G. R. (2015). Central american biomass burning smoke can increase tornado severity in the u.s. *Geophys. Res. Lett.*, *42*, 956–965. Retrieved from https://doi.org/10.1002/2014GL062826

Sayer, A. M., Munchak, L. A., Hsu, N. C., Levy, R. C., Bettenhausen, C., & Jeong, M.-J. (2014). Modis collection 6 aerosol products: Comparison between aqua's e-deep blue, dark target, and "merged" data sets, and usage recommendations. *J. Geophys. Res.: Atmos*, *119*, 13,965-13,989. Retrieved from https://doi.org/10.1002/2014JD022453

Stefanova, L., Meixner, J., Wang, J., Ray, S., Mehra, A., Barlage, M., ... Zheng, W. (2022). *Description and results from ufs coupled prototypes for future global, ensemble and seasonal forecasts at ncep.* Office Note 510, NOAA. Retrieved from https://doi.org/10.25923/knxm-kz26

Stier, P., Feichter, J., Kinne, S., Kloster, S., Vignati, E., Wilson, J., ... Petzold, A. (2005). The aerosol-climate model echam5-ham. *Atmos. Chem. Phys.*, *5*, 1125–1156. Retrieved from http://www.atmos-chem-phys.net/5/1125/2005/

Sun, D. L., Lau, K. M., & Kafatos, M. (2008). Contrasting the 2007 and 2005 hurricane seasons: Evidence of possible impacts of saharan dry air and dust on tropical cyclone activity in the atlantic basin. *Geophys. Res. Lett.*, *35*, L15405. Retrieved from doi:10.1029/2008GL034529

Tolman, H. L., Balasubramaniyan, B., Burroughs, L. D., Chalikov, D. V., Chao, Y. Y., Chen, H. S., & Gerald, V. M. (2002). Development and implementation of wind generated ocean surface wave models at ncep. *Weather and Forecasting*, *17*, 311-333.

Tompkins, A. M., Cardinali, C., Morcrette, J.-J., & Rodwell, M. (2005). Influence of aerosol climatology on forecasts of the african easterly jet. *Geophys. Res. Lett.*, *32*, L10801. Retrieved from doi:10.1029/2004GL022189

Twomey, S. (1974). Pollution and the planetary albedo. *Atmospheric Environment*, *8*, 1251–1256.

Vogel, A., Alessa, G., Scheele, R., Weber, L., Dubovik, O., North, P., & Fiedler, S. (2022). Uncertainty in aerosol optical depth from modern aerosol-climate models, reanalyses, and satellite products. *Journal of Geophysical Research: Atmospheres*, *127*, e2021JD035483. doi: doi.org/10.1029/2021JD035483

Wielicki, B. A., Barkstrom, B. R., Harrison, E. F., Lee, R. B., Smith, G. L., & Cooper, J. E. (1996). Clouds and the earth's radiant energy system (ceres): An earth observing system experiment. *Bulletin of the American Meteorological Society*, *77*(5), 853-868. doi: 10.1175/1520-0477(1996)077⟨0853:CATERE⟩2.0.CO;2

Xian, P., Reid, J. S., Hyer, E. J., Sampson, C. R., Rubin, J. I., Ades, M., ... Zhang, J. (2019). Current state of the global operational aerosol multi-model ensemble: An update from the international cooperative for aerosol prediction (icap). *Quart. J. Roy. Meteor. Soc.*, *145*, 176–209. doi: doi.org/10.1002/qj.3497

Zhang, L., Montuoro, R., McKeen, S. A., Baker, B., Bhattacharjee, P. S., Grell, G. A., ... Li, F. (2022). Development and evaluation of the aerosol forecast member in ncep's global ensemble forecast system (gefs-aerosols v1). *Geosci. Model Dev.*, *15*. Retrieved from `https://doi.org/10.5194/gmd-15-5337-2022`